Nanoscale Surface Pattern Evolution in Heteroepitaxial Bimetallic Films

Nasser Mohieddin Abukhdeir[†] and Dionisios G. Vlachos*

Department of Chemical Engineering, University of Delaware, Newark, Delaware 19716, United States. [†]Present address: Department of Chemical Engineering, University of Waterloo, Waterloo, Ontario N2L 3G1, Canada.

ABSTRACT Nanoscale self-assembly dynamics of submonolayer bimetallic films was studied through simulation of a coarse-grained mesoscopic model. Simulations predict a phase transition sequence (hexagonal→stripe→inverse hexagonal) consistent with experimental observations of Pb/Cu(111) heteroepitaxial growth. Post-transition ordering dynamics of hexagonal and inverse hexagonal patterns was simulated and quantified in order to predict pattern quality and evolution mechanisms. Correlation length scaling laws and nanoscale evolution mechanisms were predicted through simulation of experimentally relevant length ($\approx$1 μm^2) and time scales, with findings supporting evidence of universal pattern behavior with other hexagonal systems. Results provide detailed dynamics and structure of this novel self-assembly process applicable to the design and optimization of functional bimetallic materials, such as bimetallic catalysts.

KEYWORDS: self-assembly · pattern formation · thin films · hexagonal order · simulation

Self-assembly offers an economically scalable method of synthesis of functional materials *via* "bottom-up" manufacturing. Recent observations of nanoscale surface pattern formation[1,2] have inspired multidisciplinary research into applications of these phenomena. New applications based upon these self-assembly processes require a better understanding of the complex dynamic pathways that affect equilibrium pattern features and quality. This is challenging, in that self-assembled phase transformations are both dynamic and multiscale, ranging from nanoscale pattern features and defects to meso- and macroscale pattern orientational/translational order.

Surface self-assembly research has been predominantly focused on diblock copolymer thin films[1,2] for use in the semiconductor industry. Other material systems that exhibit surface self-assembly are of recent interest for novel nanofabrication applications in the semiconductor and catalysis areas. Examples of these techniques being researched include quantum dot formation,[3] electrochemical etching,[4] and submonolayer (ML) heteroepitaxial growth.[5,6] Recent observations of pattern formation in sub-ML films of Pb on a Cu(111) substrate[5] open up new opportunities for applications of nanofeatured bimetallic materials. In particular, this type of self-assembly is of interest for the development of new classes of bimetallic catalysts[7] with precise control over catalyst structure, and subsequent reactive properties, *via* manipulations of the self-assembly process during heteroepitaxial growth.

The mechanism of heteroepitaxial pattern formation is also interesting from a fundamental point of view due to the presence of "soft" ($\sim k_BT$) interactions in materials that are typically dominated by "hard" interactions (resulting in *crystallization*). As opposed to close-packing of ordered phases of colloids and metal crystals, this phenomenon is driven by soft interactions of collective domains of adsorbed Pb atoms which interact both with attractive metallic bonding and repulsive surface strain fields[8] induced by the lattice-mismatch with the underlying Cu(111) substrate. This combination of short-range attractive and long-range repulsive interactions is a well-known recipe for pattern-forming systems.[9,10]

In the bimetallic Pb/Cu(111) system, the pattern-forming domains are observed to be large submonolayer clusters of metal atoms (Figure 1), which are expected to exhibit novel collective and solitary diffusive modes coupled to pattern evolution. Little is known about the structure and dynamics of this novel pattern formation mechanism. Other pattern-forming systems with different structure and interactions on the microscopic level, but shared phase-order symmetries, have been found to exhibit "universal" pattern dynamics[11] following an order–disorder transition (ODT). Thus, determining if this broad class of materials also exhibits universality could link much past research of other self-assembled materials to new materials and applications, accelerating surface self-assembly-based manufacturing.

Past approaches to modeling surface pattern formation include the phase-field

* Address correspondence to vlachos@udel.edu.

Received for review May 29, 2011 and accepted July 28, 2011.

Published online August 05, 2011
10.1021/nn201979q

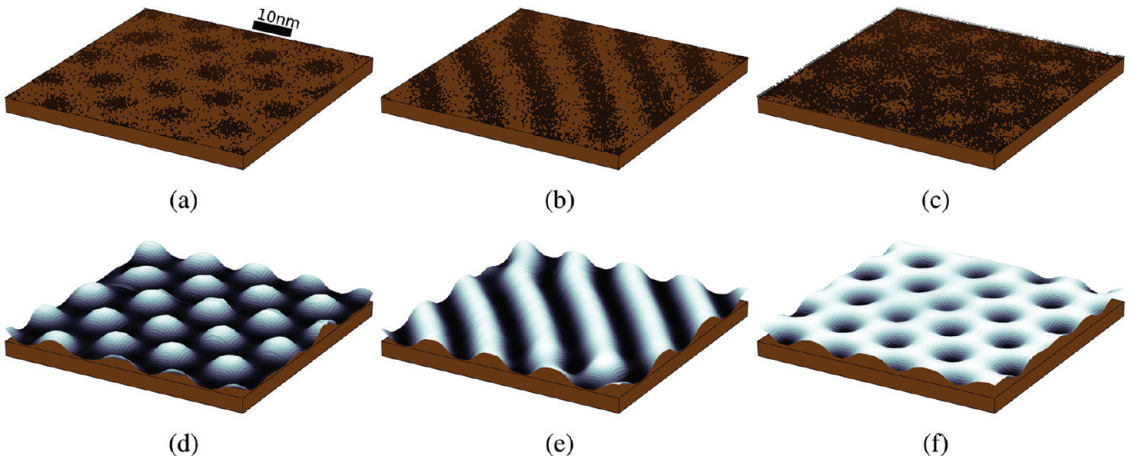

Figure 1. Schematics of different surface patterns observed in heteroepitaxially formed submonolayer Pb (• symbol) films on a Cu(111) substrate, (a) hexagonal, (b) stripe, and (c) inverse hexagonal and the resulting coarse-grained mean-field representation of each surface pattern (d–f) used in simulations.

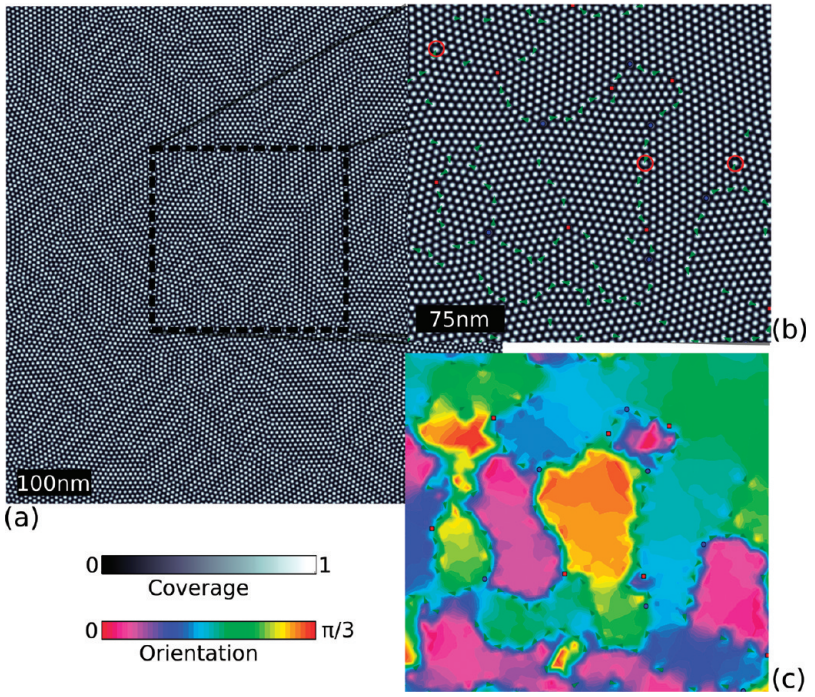

Figure 2. (a) Sample hexagonally ordered submonolayer (c_0 = 0.35 ML) film with image analysis of a subdomain shown in (b); (b) postprocessing results showing +/− disclination defects (red squares and blue circles, respectively), dislocations (green arrows), and anisometric pattern features (red circles); (c) postprocessing results showing local hexagonal domain orientation (with respect to a reference angle) and defects.

model of Suo and Lu.[8] Linear and nonlinear analysis of this model[12] has shown good qualitative agreement with phase equilibrium behavior in the experimental Pb/Cu(111) system.[5] In this work, recent theoretical advances in coarse-graining of Ising-type microscopic lattice models[13] are leveraged to simulate the range of surface patterns utilizing a single coherent theoretical basis. This approach has been shown to allow flexibility in including multiple microscopic processes/species[14] (diffusion, adsorption/desorption, reaction) and dynamics[15] (Metropolis, Arrhenius). Furthermore, through spatial and temporal coarse-graining,[13] this theoretical approach provides a framework for hierarchical multiscale simulation. The presently used coarse-grained "mesoscopic" formulation enables long-time/large length-scale simulations[16] of the heteroepitaxial pattern evolution dynamics while retaining most of the physics of the underlying microscopic model.

In this work, we focus on simulation of sub-ML surface coverages in the stable hexagonal and inverse hexagonal regimes. For most applications, the desired pattern quality involves the formation of large periodic

domains with few or no defects. Simulations of large ≈1 μm^2 surfaces over long times (with respect to pattern evolution) are combined with quantitative pattern analysis tools (developed in-house) using bond-orientational order concepts to characterize simulation domains.[17,18] Pattern quality evolution, measured *via* correlation lengths and defect densities, is used to determine scaling laws which are compared to similar results for other material systems (block copolymer surface self-assembly) to assess universality. Observations from the spatial evolution of the pattern are then presented, showing the dominant mechanisms for pattern evolution.

Model, Pattern Analysis, and Defects. Figure 2a shows a sample 1 μm^2 hexagonally ordered simulation domain predicted by the mesoscopic model with surface coverage of $c_0 = 0.35$ ML. The mesoscopic (diffusion) model is described elsewhere[13−15] (see Methods section). Simulations were performed at a constant dimensionless interaction potential:

$$\tilde{J}(T, c_0) = \beta J_0 c_0 (1 - c_0) \quad (1)$$

where $\beta = (k_B T)^{-1}$ and J_0 is the interaction strength between adatoms (see eq 3). Linear analysis of the mesoscopic model[12,19] was previously used to determine the critical $\tilde{J}$ value below which patterns form, which was found to depend on coverage and the difference in strength between attractive and repulsive interactions. Simulations were performed with $\tilde{J} = 0.0455$, which is below the critical value for pattern formation determined in ref 19.

Simulations predict that the hexagonal phase consists of interacting "islands" of microphase-separated adsorbed atoms (Figure 1). An example domain is shown in Figure 2a, with a magnified subdomain (Figure 2b) identifying hexagonal defect structures which were determined through postprocessing. Also highlighted in Figure 2a are anisometric pattern structures in areas of increased local strain in and near defects. Such hexagonal domain morphology was observed in the experimental system *via* low-energy electron microscopy (LEEM)[5,20] for both the hexagonal and inverse hexagonal phases.

In order to quantify the pattern quality, hexagonal islands were identified *via* image processing. To take into account the existence of anisometric hexagonal islands, a characteristic length of the pattern features λ_c was computed using the dominant Fourier mode of the coverage.[16,18] Hexagonal islands with a major axis greater than 150% of λ_c were treated as two separate hexagonal islands. The centers of these two islands correspond to the focii of an ellipse best-fit to the original hexagonal island. Bond-orientational order theory[21] was then used to determine local orientational order of the hexagonal domains.[18,22,23] Hexagonal defects were identified by counting nearest neighbors determined through Delaunay triangulation. Orientational defects, disclinations, involve a rotation of the domain by $\pm\pi/3$. These defects are identified by hexagonal features with five (+ disclination) or seven (− disclination) nearest neighbors. Translational defects, dislocations, involve a creation or annihilation of a hexagonal row. These defects are identified as pairs of adjacent oppositely charged disclinations. Thus, only "free" disclinations are identified, which have no oppositely charged neighbors. Figure 2b shows both disclinations (points) and dislocations (vectors/arrows) in the highlighted subdomain.

In simulations of the stable hexagonal regime, disclination defects are predominantly found to be attached to hexagonal grain boundaries which are composed of strings of dislocations. Grain boundaries are clearly visible, but further postprocessing is needed to clearly identify grain orientation and interfaces. Figure 2c shows the resulting hexagonal orientation field $\theta(x,y)$ determined using the line segment orientation between nearest hexagonal neighbors. Through visual representation of the hexagonal (and inverse hexagonal) domains, tracking the evolution of hexagonal grains and resulting defect interactions is feasible. Consistent with past simulations of hexagonal phases in block copolymer (BCP) surface self-assembly,[18,23] two types of grain boundaries (GBs) are observed: small- and large-angle (SAGB and LAGB). They are distinguished by the degree of change in hexagonal orientation across them. SAGBs impart a small or gradual change in hexagonal orientation, shown as a gradual color gradient in Figure 2c. LAGBs impart a large change in orientation, which is shown as a sharp interface, typically bisected by a string of dislocation defects (arrows shown in Figure 2c).

A sample subdomain of the inverse hexagonal phase ($c_0 = 0.75$ ML) is shown in Figure 3a with defects identified using the same convention as the hexagonal phase. The inverse hexagonal phase consists of a matrix of microphase-separated adsorbed atoms with voids or "holes" composing the hexagonal pattern (Figure 1c). As opposed to observations in BCP surface self-assembly, in the bimetallic system, the inverse hexagonal phase is not the symmetric opposite of the hexagonal phase. Thus the evolution of the hexagonal and inverse hexagonal patterns through the translation of islands/holes involves very different diffusion mechanisms, which will be quantified through the evolution of the overall pattern order/quality. Few past simulations have captured inverse hexagonal phase ordering, and these simulations, to our knowledge, present the first results of quantitative pattern dynamics for this phase.

The inverse hexagonal pattern is also observed to have strain-induced variation in individual hexagonal features. This is mainly localized to regions around disclination defects, and large aspect ratio features are

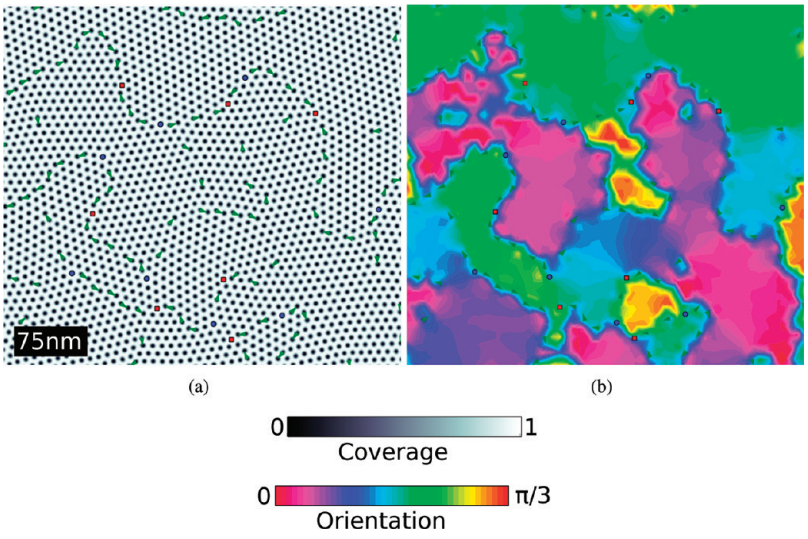

Figure 3. Sample inverse hexagonal ordered submonolayer (c_0 = 0.75 ML) film from image analysis of a subdomain with (a) +/− disclination defects (red squares and blue circles, respectively) and dislocations (green arrows) shown; (b) local hexagonal domain orientation with defects.

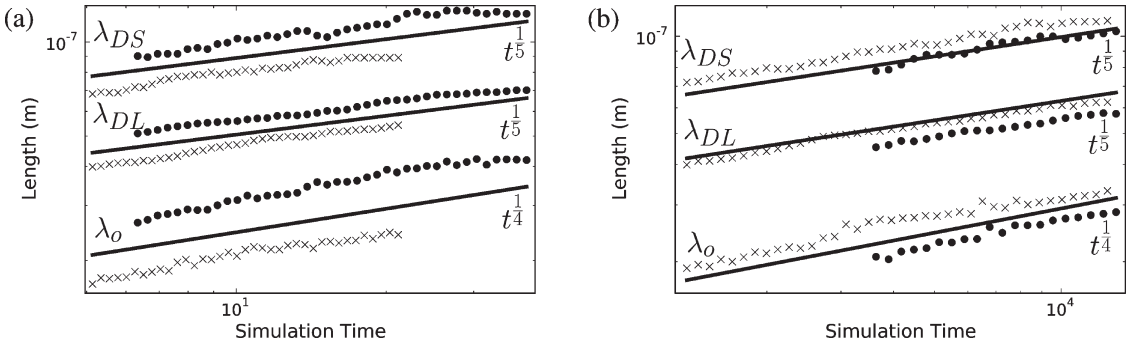

Figure 4. Orientational correlation length λ_0 and defect densities, $\lambda_{DS} = \rho_{DS}^{-1/2}$ and $\lambda_{DL} = (p\rho_{DL})^{-1}$, *versus* simulation time for both Metropolis and Arrhenius diffusions dynamics for the (a) disordered→hexagonal and (b) disordered→inverse hexagonal transitions. Best fit exponents t^n for both hexagonal and inverse hexagonal patterns with both Metropolis (●) and Arrhenius (×) dynamics (Table 1) are approximately $\lambda_0 \propto t^{1/4}$, $\lambda_{DS} \propto t^{1/5}$, and $\lambda_{DL} \propto t^{1/5}$.

not observed prevalently as with the hexagonal phase. Again, disclination defects are observed to be predominantly associated with grain boundaries. Figure 3b shows the computed bond-orientation field for the inverse hexagonal domain where both SAGBs and LAGBs are also observed.

Pattern Quality Evolution and Scaling Laws. In order to quantitatively determine how the quality of the pattern evolves following the ODT, pattern evolution was characterized through the orientational correlation function:[18]

$$\xi_6(r, t) = \langle e^{6i[\theta(r+r', t) - \theta(r', t)]} \rangle \qquad (2)$$

where θ is the local hexagonal orientation. The orientational correlation length was determined by fitting $\xi_6(r,t)$ to an exponential function $\exp(-r/\lambda_0)$.[18] Long-time simulations were performed on large periodic domains of 1 μm^2 and post-ODT pattern evolution analyzed for dynamic scaling behavior. Two sets of simulations were performed using different approximations for the adsorbate mobility corresponding to different diffusion dynamics: Metropolis and Arrhenius.[15] Metropolis dynamics approximates the local mobility as $\mu[c] = De^{-U_0}\beta c(1 - c)$, and the barrier for diffusion is constant. Arrhenius dynamics takes into account the local potential energy barrier to diffusion $\mu[c] = De^{-U(x,y)}\beta c(1 - c)$. Simulation sets were performed for both patterns (hexagonal and inverse hexagonal) and dynamics (Metropolis and Arrhenius) using identical (within the set) disordered initial conditions (see the Methods section).

Figure 4 shows sample postprocessing results of the correlation length evolution in the stable hexagonal (Figure 2a) and inverse hexagonal (Figure 3a) regimes. Power law best-fits with time, $\propto t^n$, were computed for each simulation and are shown in Table 1. In addition to the directly computed correlation lengths λ_0, approximate characteristic lengths were determined using disclination (ρ_{DS}) and dislocation (ρ_{DL}) densities.[22] These approximate length scales correspond to the

TABLE 1. Power Law Best-Fit Results

stable pattern	diffusion dynamics	λ_0	$\lambda_{DS} = \rho_{DS}^{-1/2}$	$\lambda_{DL} = (p\rho_{DL})^{-1}$
hexagonal	Metropolis	0.25	0.20	0.23
hexagonal	Arrhenius	0.27	0.20	0.18
inverse hexagonal	Metropolis	0.24	0.21	0.20
inverse hexagonal	Arrhenius	0.26	0.21	0.23

average distance between disclinations $\lambda_{DS} = \rho_{DS}^{-1/2}$ and the average grain size $\lambda_{DL} = (p\rho_{DL})^{-1}$, where p is the average distance between dislocations in a grain boundary.[22] Comparison between directly computed orientational correlation length λ_0 and approximate characteristic lengths using defect densities provides insight into the pattern evolution process. For example, for striped BCP surface self-assembly, it was shown that the interaction of disclination defects drives the ordering process through an equivalence of the scaling of λ_0 and λ_{DS}.[1,24,25]

These results support three major observations. First, they predict that heteroepitaxial pattern formation does exhibit universal behavior where the pattern evolution dynamics agrees with other hexagonal surface-pattern-forming systems (BCP surface self-assembly).[22,23] Second, the pattern dynamics of the inverse hexagonal phase is identical to that of the hexagonal phase, in spite of the previously mentioned difference in the microscopic structure. Third, diffusion dynamics does not affect the scaling behavior of the pattern dynamics.

Past experimental[22] and simulation[23] studies of (spherical) BCP surface self-assembly have shown that BCP self-assembly exhibits essentially two-dimensional hexagonal order. These past studies, using similar hexagonal order postprocessing techniques, have found that the dynamics of the surface pattern evolution evolves in time with power law dependences of $\lambda_0 \approx t^{1/4}$, $\lambda_{DS} \approx t^{1/5}$, and $\lambda_{DL} \approx t^{1/5}$. The present results show that the heteroepitaxial hexagonal surface patterns show universal behavior in agreement with observations of the BCP hexagonal phases. Since diffusion dynamics is found to have no effect on the growth kinetics of either phase, the present results further support that phase-order symmetries are the sole indicator of pattern dynamics scaling.

For the inverse hexagonal transition, there is no past experimental or simulation data with which to compare pattern dynamics as these results are the first (to our knowledge). This phase is observed to have identical scaling behavior, albeit over longer time scales. These slower dynamics, at identical reduced temperature, are possibly related to the larger diffusive flux of atoms required for the hexagonal holes to move, displacing the adsorbed phase. In contrast to the hexagonal phase, which involves the translation of hexagonal "islands" in a particle-depleted matrix phase, inverse hexagonal coarsening involves the translation of hexagonal holes in a particle-rich matrix phase, which is less energetically favored.

Hexagonal Pattern Evolution Mechanisms. Upon the basis of the above results, simulations of the heteroepitaxial system should yield pattern evolution mechanisms comparable to past results from BCP surface self-assembly. Past experimental[22] and theoretical[23] observations of a two-dimensional hexagonal phase revealed that the main mechanism for pattern evolution was the "zipping-up" of a single small hexagonal grain entrained between two larger hexagonal grains. This mechanism was also observed in the present simulations of the heteroepitaxial system, with an example depicted in Figure 5. As shown in the example, this process involves the motion of two "forks" in the grain boundary that separate the larger two hexagonal grains. These two forks contain the smaller grain which shrinks as the forks approach each other. Each fork has an oppositely charged hexagonal disclination in its vicinity, such that this motion brings them together and is concluded by the annihilation of the pair. In the current simulations shown in Figure 5, this mechanism was found to actively involve only one of the large grains (grain C) with the smaller grain (grain B), while the neighboring large grain (grain A) remains locally static in size. This lack of participation of one of the neighboring grains was consistently observed in different simulations.

The previously observed mechanism was found to occur once hexagonal grain sizes were sufficiently large, that is, typically with a length scale of an order of magnitude greater than characteristic length scale ($\lambda_c \approx 9$ nm from simulations). Preceding and also during this regime of pattern coarsening, a more complex set of mechanisms is observed whereby hexagonal grains grow through "ripening" of earlier-stage hexagonal domains with poorly defined grain boundaries (see Figure 2c and Figure 3b). Such poorly defined, or diffuse, grain boundaries within a single grain or between multiple grains were also observed in past studies.[22,23] These newly found mechanisms typically resulted in the refinement of a single hexagonal grain into a larger one with more well-defined GBs.

Growth *via* ripening was observed to occur in two general variations with diffuse GB areas either entrained within a large hexagonal grain (Figure 5) or on its edge (Figure 6). Evolution of the internal and edge types of grain refinement are shown in Figure 5a–c and Figure 6a–c, respectively. Once this process initiates, it occurs solely through the motion and annihilation of dislocations within the diffuse boundary. Figure 5a–c shows the internal-type growth *via* ripening where an entrained misoriented subgrain shrinks through the collapse of a GB loop *via* dislocation annihilation events. Figure 6a–c shows the edge-type mechanism, where dislocations coalesce in a

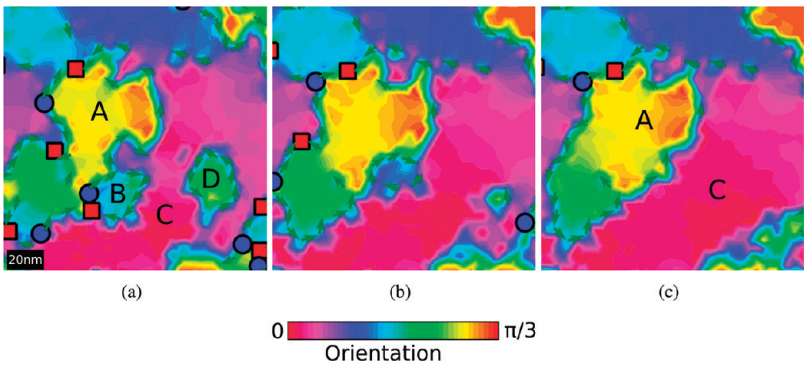

Figure 5. Evolution of an inverse hexagonal simulation (Metropolis dynamics) subdomain where grains A/B exhibit the zipping-up mechanism and grains C/D entrained ripening: (a) $t = 6 \times 10^3$, the initial configuration with grain A sharing a boundary with B and grain D entrained in C, (b) $t = 5 \times 10^4$, both grains B and D shrink through the zipping-up mechanism, where oppositely charged dislocations within a GB dislocation loop annihilate, and (c) $t = 1 \times 10^5$, grains A and C have fully absorbed grains B and D, respectively.

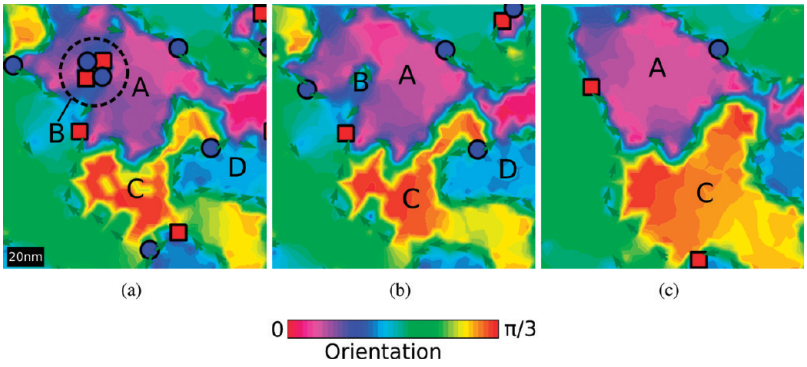

Figure 6. Evolution of hexagonal subdomain evolution (Metropolis dynamics) showing two additional examples of the edge ripening mechanism: (a) $t = 20$ the initial configuration with grains A and C sharing GBs with grains B and D, (b) $t = 35$, grain A begins to absorb grain B following the annihilation of a disclination quadrupole in their shared GB and grain C begins to absorb grain D through the zipping up mechanism, (c) $t = 150$, grain A has fully absorbed grain B while grain C continues to absorb grain D.

poorly ordered region. This coalescence results in the transition from diffuse to clearly defined GBs. This mechanism is similar to the zipping-up process observed in hexagonal BCP phases, where here a single larger hexagonal grain exists instead of two neighbors.

While disclinations serve to stabilize GBs following ripening and splitting events, the annihilation of oppositely charged disclination pairs was also observed to initiate the majority of the evolution mechanisms observed. As pairs of disclinations annihilate, the hexagonal domain relaxes locally, enabling the translation of neighboring defects and GBs.

SUMMARY

In summary, novel surface self-assembly of heteroepitaxially formed bimetallic thin films was simulated using a coarse-grained "mesoscopic" model. This computational approach was found to qualitatively agree with experimental LEEM images of Pb/Cu(111) heteroepitaxial pattern formation including phase transition sequence and morphology. Pattern evolution of stable hexagonal and inverse hexagonal phase-ordered regimes were simulated. We found that these phases exhibit universal dynamics independent of microscopic morphology (hexagonal *versus* inverse hexagonal) and surface diffusion dynamics (locally constant *versus* locally varying mobility). These results provide further support for the existence of universal pattern dynamics dependent solely on symmetries of the ordered phase.

Postprocessing of simulation results was used to identify specific mechanisms of pattern ordering. New mechanisms and insight into past observations of hexagonal phase ordering were found, showing that the dynamic path to increased hexagonal ordering, and pattern quality, is complex. Simulated

TABLE 2. Material Parameters

variable	value	description
T	650 K	temperature
a	5 Å	lattice spacing
J_0	1.80×10^{-21} J	isotropic potential
h	-1.25×10^{-19} J	binding energy
r_a	2.24 nm	attraction length scale
r_r	5 nm	repulsion length scale

hexagonal grain interactions revealed that pair interactions of grains, with nonparticipating neighboring grains, are the dominant mode of hexagonal grain growth and increasing pattern quality. This computational approach and results motivate the future use of optimal control techniques to determine operating parameters (*e.g.*, temperature, coverage, adsorption rate) for the development of nanomanufacturing processes of high-quality bimetallic patterned surfaces for catalytic and other applications.

METHODS

Heteroepitaxy Model. The prototype experimental system for which the mesoscopic diffusion model was initially proposed is Pb/Cu(111) heteroepitaxial pattern formation.[5,20,26,27] Past work has modeled this material system using an interacting particle (IP) mesoscopic diffusion model[13,19] with particle/particle interactions consisting of short-range attractive and long-range repulsive Gaussian components:

$$J(r) = -J_0\left(e^{-\left(\frac{r}{r_a}\right)^2} - \chi e^{-\left(\frac{r}{r_r}\right)^2}\right) \quad (3)$$

where J_0 is the strength of the isotropic potential, χ is the repulsion strength parameter [0,1], and r_a/r_r is the attractive/repulsive length scale. The free energy for the mesoscopic model was introduced in refs 13 and 15:

$$E[c] = \frac{1}{2}\int U(r)c(r)dr + \frac{1}{\beta}\int [c\ln c + (1-c)\ln(1-c)]dr \quad (4)$$

where $c(t,x,y)$ is the local particle coverage field ranging from $0 \rightarrow 1$, $\beta = (k_B T)^{-1}$, $U(t,x,y) = J(c+h)$ is the interaction energy, and h is an external field term. The free energy eq 4 is composed of energetic (term 1) and entropic (term 2) contributions. This free energy equation enables the mesoscopic model to be formulated in the familiar Cahn–Hilliard form for a constrained/conserved order parameter:

$$\frac{\partial c}{\partial t} = -\nabla\cdot\left\{-\mu[c]\nabla\left(\frac{\delta E[c]}{\delta c}\right)\right\} \quad (5)$$

The mobility term $\mu[c]$ is $\mu[c] = De^{-U_0}\beta c(1-c)$ (Metropolis) and $\mu[c] = De^{-U_0}\beta c(1-c)$ (Arrhenius), where $U_0 = c_0\int J(r)dr + h$ is a constant. Both Metropolis and Arrhenius diffusion dynamics take into account the energy difference between states. Upon coarse-graining of the microscopic model, Arrhenius dynamics results in a coverage dependent energy barrier to diffusion whereas Metropolis does not. As with the interaction potential (eq 3), the diffusion coefficient is directly related to parameters of the underlying microscopic model, $D = (1/4)\Gamma a^2$, where Γ is the transition probability rate, a is the microscopic lattice constant, and the factor of 1/4 is determined by the underlying lattice.

Simulation Conditions. The numerical methods used are detailed in ref 16. In summary, the Fourier spectral method was used for spatial discretization, and an implicit variable-order backward differencing time-intregation method was used with an underlying Newton–Krylov nonlinear solver (SUNDIALS, see ref 28). This novel numerical approach enables stable long-time integration and access to large length scales required for this study. The simulation domain was a square with dimension of 1 μm^2. A uniformly discretized grid of 1154^2 nodes was used with periodic boundary conditions imposed by the Fourier spectral method. Simulation times are reported in dimensionless units $\tau = 4/\Gamma$. Simulation parameters are given in Table 2 where temperature for each simulation was determined using a fixed dimensionless interaction strength $\beta J_0 c_0(1-c_0) = 0.0455$, below the critical interaction strength required for pattern formation with $\chi = 0.5$.[19]

Initial conditions representative of the unstable disordered phase were used of the form:

$$c_{ij}(t=0) = c_0 + N_{ij}(\mu, \sigma^2) \quad (6)$$

where $c_0^{hex} = 0.35$ ML and N is a normally distributed random variable on the interval [−0.1,0.1] with mean $\mu = 0$ and variance $\sigma^2 = 0.01$. These initial conditions were used for the hexagonal phase simulations. Initial conditions for inverse hexagonal phase simulations employed a continuation method where early ($t = 1$) partially formed hexagonal phase domains c_{ij}^{hex} were used as initial conditions after renormalization to $c_0^{inv} = 0.75$ ML:

$$c_{ij}(t=0) = c_{ij}^{hex} + \frac{\Delta c}{1-c_0^{hex}}(1-c_{ij}^{hex}) \quad (7)$$

where $\Delta c = c_{ij}^{inv} - c_{ij}^{hex}$.

Phase-Order Characterization. Quantification of hexagonal and inverse hexagonal domain order was approximated using bond-orientational order (BOO) concepts.[21] This approach has been used for other systems exhibiting two-dimensional hexagonal ordering, spherical block copolymer thin film self-assembly.[18,22]

Each simulation snapshot was digitized to identify individual pattern features using the magnitude of the gradient $|\nabla c|$ with a threshold of the spatially averaged mean value. The centers-of-mass of the objects in the resulting digitized image were then used as discrete points associated with each hexagonal feature. Delaunay triangulation was then employed to determine nearest neighbors and to construct an undirected graph for BOO analysis. The resulting undirected graph was used to determine the local orientational order parameter:[17]

$$\Psi_n = \frac{1}{N}\sum_N \exp(ni\phi) \quad (8)$$

where $n = 6$ for hexagonal and inverse hexagonal order and N is the number of local nearest neighbors. Candidate disclination defects were identified by nodes with 5 (+) and 7 (−) neighbors. Dislocations were then identified as pairs of neighboring plus and minus disclinations through computing the maximum matching[29] of the undirected graph. Remaining unpaired disclinations were then counted as "free".

Acknowledgment. This work was supported, in part, by the National Science Foundation (USA, CMMI-0835673) and the Natural Science and Engineering Research Council of Canada (NMA).

Supporting Information Available: Animation files of pattern domain evolution used in Figure 4 are provided in compressed MPEG-4 format. Data files are named according to pattern (hexagonal or inverse hexagonal), diffusion dynamics (Metropolis or Arrhenius), and data-type (coverage field or local bond-orientation field). This material is available free of charge *via* the Internet at http://pubs.acs.org.

REFERENCES AND NOTES

1. Harrison, C.; Adamson, D. H.; Cheng, Z.; Sebastian, J. M.; Sethuraman, S.; Huse, D. A.; Register, R. A.; Chaikin, P. M. Mechanisms of Ordering in Striped Patterns. *Science* **2000**, *290*, 1558–1560.
2. Marencic, A. P.; Register, R. A. Controlling Order in Block Copolymer Thin Films for Nanopatterning Applications. *Annu. Rev. Chem. Biomol. Eng.* **2010**, *1*, 277–297.
3. Ross, F. M.; Tersoff, J.; Tromp, R. M. Coarsening of Self-Assembled Ge Quantum Dots on Si(001). *Phys. Rev. Lett.* **1998**, *80*, 984–987.

4. Singh, S.; Barden, W. R. T.; Kruse, P. Nanopatterning of Transition Metal Surfaces *via* Electrochemical Dimple Array Formation. *ACS Nano* **2008**, *2*, 2453–2464.
5. Plass, R.; Last, J. A.; Bartelt, N. C.; Kellogg, G. L. Nanostructures: Self-Assembled Domain Patterns. *Nature* **2001**, *412*, 875–875.
6. Liao, S.-C.; Tsai, P.-Y.; Liang, C.-W.; Liu, H.-J.; Yang, J.-C.; Lin, S.-J.; Lai, C.-H.; Chu, Y.-H. Misorientation Control and Functionality Design of Nanopillars in Self-Assembled Perovskite-Spinel Heteroepitaxial Nanostructures. *ACS Nano* **2011**, *5*, 4118–4122.
7. Wickman, B.; Seidel, Y. E.; Jusys, Z.; Kasemo, B.; Behm, R. J. Fabrication of Pt/Ru Nanoparticle Pair Arrays with Controlled Separation and Their Electrocatalytic Properties. *ACS Nano* **2011**, *5*, 2547–2558.
8. Suo, Z.; Lu, W. Forces That Drive Nanoscale Self-assembly on Solid Surfaces. *J. Nanopart. Res.* **2000**, *2*, 333–344.
9. Wu, J.; Liu, Y.; Chen, W.-R.; Cao, J.; Chen, S.-H. Structural Arrest Transitions in Fluids Described by Two Yukawa Potentials. *Phys. Rev. E* **2004**, *70*, 050401.
10. Shin, H.; Grason, G. M.; Santangelo, C. D. Mesophases of Soft-Sphere Aggregates. *Soft Matter* **2009**, *5*, 3629.
11. Cross, M. C.; Hohenberg, P. C. Pattern Formation Outside of Equilibrium. *Rev. Mod. Phys.* **1993**, *65*, 851.
12. Hu, S.; Nathan, G.; Hussain, F.; Kouri, D. J.; Sharma, P.; Gunaratne, G. H. On Stability of Self-Assembled Nanoscale Patterns. *J. Mech. Phys. Solids* **2007**, *55*, 1357–1384.
13. Vlachos, D.; Katsoulakis, M. Derivation and Validation of Mesoscopic Theories for Diffusion of Interacting Molecules. *Phys. Rev. Lett.* **2000**, *85*, 3898–3901.
14. Chatterjee, A.; Vlachos, D. G. Continuum Mesoscopic Framework for Multiple Interacting Species and Processes on Multiple Site Types and/or Crystallographic Planes. *J. Chem. Phys.* **2007**, *127*, 034705.
15. Katsoulakis, M. A.; Vlachos, D. G. In *Dispersive Transport Equations and Multiscale Models*; Ben-Abdallah, N., Ed.; Springer: Berlin, 2004; p 179.
16. Abukhdeir, N. M.; Vlachos, D. G.; Katsoulakis, M.; Plexousakis, M. Long-Time Integration Methods for Mesoscopic Models of Pattern-Forming Systems. *J. Comput. Phys.* **2011**, *230*, 5704–5715.
17. Brock, J. D. In *Bond-Orientational Order in Condensed Matter Systems*; Strandburg, K. J., Ed.; Springer-Verlag: Berlin, 1992.
18. Yokojima, Y.; Shiwa, Y. Hydrodynamic Interactions in Ordering Process of Two-Dimensional Quenched Block Copolymers. *Phys. Rev. E* **2002**, *65*, 056308.
19. Chatterjee, A.; Vlachos, D. G. Systems Tasks in Nanotechnology *via* Hierarchical Multiscale Modeling: Nanopattern Formation in Heteroepitaxy. *Chem. Eng. Sci.* **2007**, *62*, 4852–4863 19th International Symposium on Chemical Reaction Engineering - From Science to Innovative Engineering—ISCRE-19.
20. Plass, R.; Bartelt, N. C.; Kellogg, G. L. Dynamic Observations of Nanoscale Self-Assembly on Solid Surfaces. *J. Phys.: Condens. Matter* **2002**, *14*, 4227.
21. Strandburg, K. J., Ed. *Bond-Orientational Order in Condensed Matter Systems*; Springer-Verlag: Berlin, 1992.
22. Harrison, C.; Angelescu, D.; Trawick, M.; Cheng, Z.; Huse, D.; Chaikin, P.; Vega, D.; Sebastian, J.; Register, R.; Adamson, D. Pattern Coarsening in a 2D Hexagonal System. *Europhys. Lett.* **2004**, *67*, 800.
23. Vega, D. A.; Harrison, C. K.; Angelescu, D. E.; Trawick, M. L.; Huse, D. A.; Chaikin, P. M.; Register, R. A. Ordering Mechanisms in Two-Dimensional Sphere-Forming Block Copolymers. *Phys. Rev. E* **2005**, *71*, 061803.
24. Harrison, C.; Cheng, Z.; Sethuraman, S.; Huse, D. A.; Chaikin, P. M.; Vega, D. A.; Sebastian, J. M.; Register, R. A.; Adamson, D. H. Dynamics of Pattern Coarsening in a Two-Dimensional Smectic System. *Phys. Rev. E* **2002**, *66*, 011706.
25. Abukhdeir, N. M.; Rey, A. D. Defect Kinetics and Dynamics of Pattern Coarsening in a Two-Dimensional Smectic-A System. *New J. Phys.* **2008**, *10*, 063025.
26. Anderson, M. L.; D'Amato, M. J.; Feibelman, P. J.; Swartzentruber, B. S. Vacancy-Mediated and Exchange Diffusion in a Pb/Cu(111) Surface Alloy: Concurrent Diffusion on Two Length Scales. *Phys. Rev. Lett.* **2003**, *90*, 126102.
27. Anderson, M. L.; Bartelt, N. C.; Feibelman, P. J.; Swartzentruber, B. S.; Kellogg, G. L. How Pb-Overlayer Islands Move Fast Enough To Self-Assemble on Pb−Cu Surface Alloys. *Phys. Rev. Lett.* **2007**, *98*, 096106.
28. Hindmarsh, A.; Brown, P.; Grant, K.; Lee, S.; Serban, R.; Shumaker, D.; Woodward, C. SUNDIALS: Suite of Nonlinear and Differential/Algebraic Equation Solvers. *ACM Trans. Math. Software* **2005**, *31*, 396.
29. Galil, Z. Efficient algorithms for finding maximum matching in graphs. *ACM Comput. Surv.* **1986**, *18*, 23–38.